Experimental Investigation of the Effect of Wavefront Aberration on the Flow Generated by Laser-Induced Breakdown

Zareb A. Noel[*], Stanislav Gordeyev[†], and R. Mark Rennie[‡]
University of Notre Dame, Notre Dame, IN, 46556

Phase aberrations and their effect on the development of flowfields caused by laser-induced breakdown is investigated. The phase aberrations are imparted onto a high-energy laser pulse at a wavelength of 1064nm using a deformable mirror. An experimental setup was devised to capture the motion of the flowfields resulting from laser-induced breakdown with phase aberration which focuses on capturing both the transverse profile, as well as the coaxial profile of the flowfield. It is shown that the laser pulse energy (181mJ) absorbed by the spark decreases significantly due to the presence of non-planar phase, which is due to spreading in the focal plane where breakdown typically occurs. Of the data collected, a single instance of Zernike $0°$Astigmatism, Zernike Y-Coma, and Zernike Spherical aberrations are investigated. The well-known Horn-Schunck optical flow method is used to analyze the shadowgraph images, producing dense optical flowfield representations of the motion. It is shown that each aberration investigated creates a unique flowfield, showing potential for hyper-specific local flow specification and the implications are further discussed.

I. Nomenclature

I	=	image or laser intensity
u	=	velocity in the x direction
v	=	velocity in the y direction
J	=	global energy functional
E_{pulse}	=	laser pulse energy
u_r	=	velocity in the radial direction
α	=	regularization parameter
k	=	iteration number
$\bar{u}, \bar{v}$	=	local spatial average of velocities
t_{pulse}	=	laser pulse duration
A_w	=	area of laser beam at tightest focus

II. Introduction

HIGH temperature plasma sparks created by focusing a high-energy laser pulse into a gas have been widely investigated for their promising aerospace applications. In studies concerning internal combustion engines, plasma sparks created by high-energy laser pulses have been studied for use as an ignition source[1, 2]. In supersonic ramjets, as investigated by Lee et al.[3], laser-induced breakdown has been shown to enhance turbulent mixing of combustible fuels with oxidizers. In external supersonic flow, the sudden deposition of energy causes local thermodynamic fluctuations that can alter shock characteristics[4, 5], leading to a weakening of shock strength, as well as significant drag reduction[6]. In more recent experiments, such as those conducted by Khamesh et al.[7] the effect of asymmetric energy deposition has been shown to create lifting forces on models in supersonic flow, showing potential for supersonic steering.

---

*Graduate Research Assistant, Department of Aerospace and Mechanical Engineering, Hessert Laboratory for Aerospace Research, AIAA Student Member.

†Associate Professor, Department of Aerospace and Mechanical Engineering, Hessert Laboratory for Aerospace Research, AIAA Associate Fellow

‡Research Professor, Department of Aerospace and Mechanical Engineering, Hessert Laboratory for Aerospace Research, AIAA Associate Fellow

While experiments have been conducted to understand how the flowfields created by laser-induced breakdown (LIB) may be used for flow control[8], very few of these experimental investigations have shown success in capturing key quantitative measurements of the flowfield generated by LIB itself[9, 10], including important scaling information regarding the laser and optical parameters. As a result, much of the recent work investigating LIB flowfields has been performed almost entirely by numerical simulations. However, due to the wide range of timescales (ns-ms) over which the flowfield develops, numerical simulation of LIB typically involves significant computational cost. As a result, tradeoffs are usually made between the efficiency of the simulation and the complexity of the simulated phenomena, often choosing the former. An example of this is the common assumption that the flowfield is axisymmetric, resulting from an axisymmetric deposition of laser energy. While useful to understand from all aspects, this is also a limitation to

The goal of this research is to investigate and develop methods for controlling the flowfield caused by LIB. The work uses the optical flow method to recover quantitative flow velocities from a series of flow visualization images. Previous research has shown that this method is capable of recovering flow velocities that yield results that agree well with experimental and numerical methods but lacks key disadvantages of both. Unlike other experimental methods, optical flow can maintain good spatio-temporal resolution while, on the other hand, requiring a much smaller computational cost.
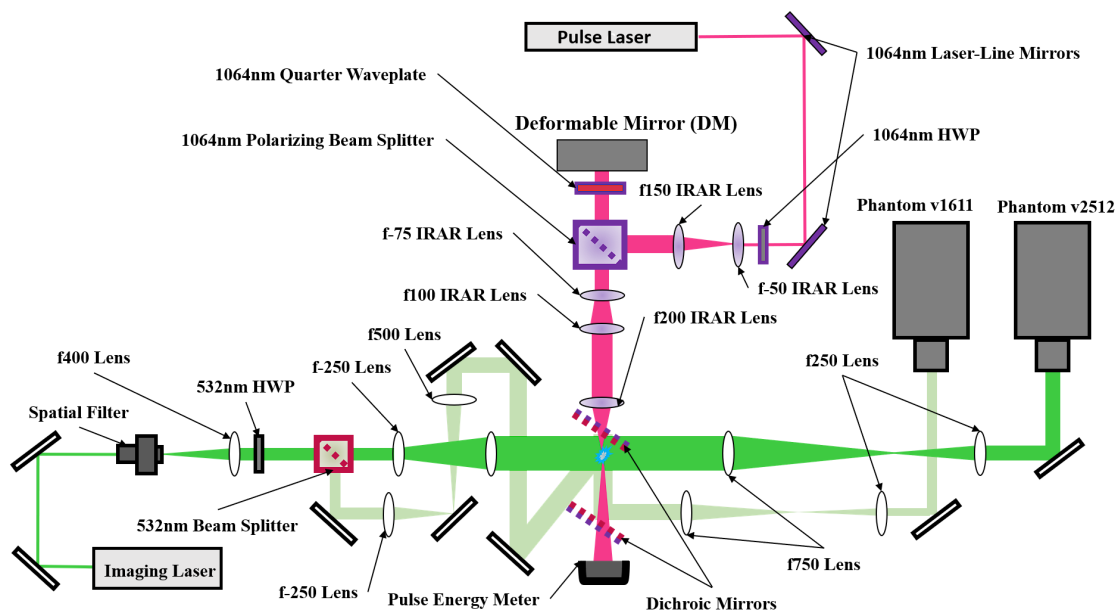

Fig. 1   Schematic of the experimental setup. The setup is split into three paths: Spark Path (SP, magenta), Transverse Imaging Path (TIP, dark green) and Coaxial Imaging Path (CIP, light green).

The optical flow method used in this research not only allows for an improved understanding of LIB flowfields that can be compared to numerical simulations, but also enables the investigation of new ways to control LIB flowfields, which can then be further explored for flow-control applications. Past experiments investigating the control of LIB flowfields most notably include the use of a dual-pulse laser setup[11], where it has been shown that the flowfield is sensitive to experimental parameters, showing potential for more specific flow control. Unfortunately, these experimental methods have not seen success in recovering quantitative information about the flowfield itself. As such, there is a need for both robust measurement and control of LIB flowfields. In this regard, this research also presents a new way to control the flowfield caused by LIB, in which a deformable mirror (DM) is used to alter the phase of the high-energy laser pulse. Changes in the phase result in changes in the spatial distribution of the plasma along the optical axis, which in turn changes the spatio-temporal development of the plasma and the resulting flowfield velocities. This concept is similar to that found in research centered around the control of laser-plasma filaments, where it has been shown that controlling the phase of a high-energy laser pulse has significant effects on the characteristics of plasma filaments created at long ranges[12]. However, laser-generated plasma filaments are uniquely different than LIB in the physical mechanism that governs their occurrence. To the knowledge of the authors, this kind of investigation into the relation between the phase aberration of a high-energy laser pulse and the resulting LIB flowfield has not yet been explored.

2

III. Experimental Procedure

The experiment was performed in a clean room with a low dust environment that reduced the probability of spark misfires due to airborne particles in the breakdown region, thus improving measurement repeatability. The schematic for the experimental setup is depicted in Fig.1. The experimental setup is split into three paths: the Spark Path (SP), the Transverse Image Path (TIP), and the Coaxial Image Path (CIP).

A. Spark Path

Laser plasma sparks were produced at the end of the SP (magenta) using a Quantel Brilliant Q-Switch Nd:YAG pulse laser operating at its fundamental frequency (1064nm) with a 5ns pulse duration and an initial beam diameter of approximately 5mm. For all data presented in this research, the delay between the Q-Switch and the flashlamp was kept constant, which yielded an average per pulse energy of approximately 181mJ. Phase aberrations were induced using a Thorlabs Piezoelectric Deformable Mirror (DM), whose actuator map is shown in Fig.2. The DM had a 18mm reflective surface with a 14mm pupil over which the 40 actuators are seated in a circular pattern, which is specifically designed to impart phase aberrations in the shape of Zernike polynomials. The first 10 Zernike polynomials are depicted in Fig.3, of which only 0°Astigmatism, Y-Coma, and Spherical aberrations were investigated in this work, in addition to the baseline case of no aberration (planar wavefront). As shown in Fig.4, the initial 5mm beam was steered into a half waveplate (HWP) situated in a rotational mount using a pair of laser-line mirrors that specifically reflect 1064nm light. The beam was then expanded using a lens pair consisting of a 50mm focal length plano-concave lens and a 150mm focal length plano-convex lens for a total magnification of 3X, resulting in a beam diameter of approximately 15mm.
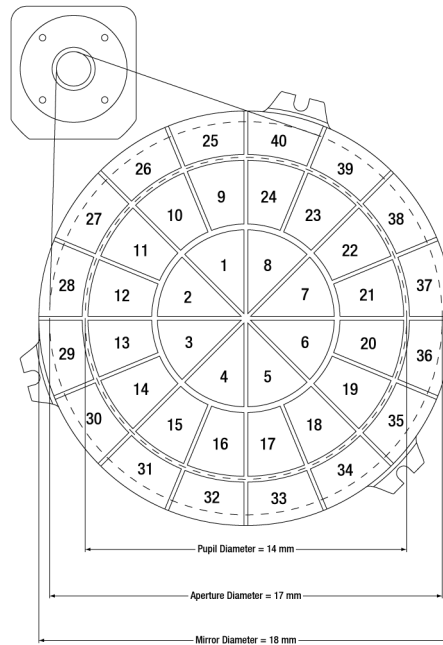

Fig. 2   Thorlabs piezoelectric deformable mirror actuator map.

A polarizing beamsplitter was used to maximize the amount of laser energy focused into the laser plasma while achieving full coverage of the DM reflective surface. This optic was used in conjunction with a half-wave plate (HWP) to tune the polarization state of the pulse, which allowed for near total reflection of the laser pulse towards the DM. As the DM will reflect all of the laser light, a quarter waveplate (QWP) was used to once again change the polarization state of the laser before reflecting off of the DM and picking up phase aberrations. By then passing through the QWP again, the polarization state of the phase-aberrated laser pulse was oriented orthogonal to its initial polarization state from the HWP so that the phase-aberrated laser pulse passed through the polarizing beam cube. In this way, optical isolation was achieved, minimizing energy losses and the risk of damaging the pulse laser.

After the DM placed a phase aberration onto the laser pulse, the pulse was then expanded to 18mm diameter using a 75mm focal length plano-concave lens and collimated using a 100mm focal length plano-convex lens. From here, the
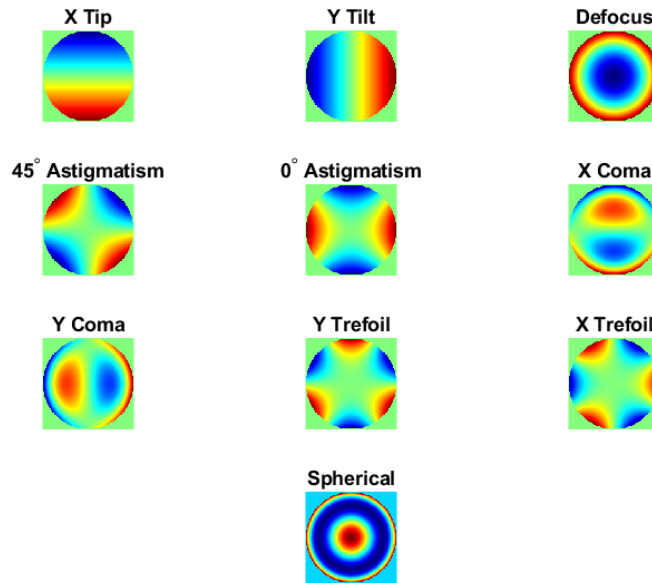
Fig. 3   First 10 Zernike modes, excluding the Piston mode.

plasma spark was produced by focusing the laser pulse using a 200mm focal length plano-convex lens. Before reaching the breakdown region, the LIB beam was passed through one dichroic mirror that transmits light at 1064nm wavelength and reflects light at 532nm wavelength. A second, identical dichroic mirror is placed after the spark breakdown location, to separate the CIP laser light and the SP laser light. As shown in numerous experimental works[13, 14], not all of the laser energy is absorbed by the plasma, and a portion of the laser light passes through the breakdown region. After the creation of the spark, the remaining laser energy was passed through the second dichroic mirror before being registered on a pulse energy meter. All lenses used on the SP had anti-reflective coatings for 1064nm to minimize reflective energy losses.

B. Transverse Image Path

Shadowgraph images of the LIB flow field in the plane orthogonal to the SP were acquired using the TIP (dark green). The imaging laser was a continuous wave (CW) laser with a central wavelength of 532nm. The beam was expanded to 25mm diameter using an objective lens with a 60X magnification and 0.85 numerical aperture (NA), as well as a 10μm pinhole that spatially filtered the beam. The output from the spatial filter was then collimated with a 400mm focal length plano-convex lens before passing through a broadband HWP and then another polarizing beamsplitter. The HWP was used to modulate the amount of light split between the TIP and CIP. A 2X beam expander consisting of a 250mm focal length and a 500mm focal length plano-convex lens, was then used to expand the beam diameter to approximately 50mm. The 50mm beam was used to collect shadowgraph images the transverse profile of the laser spark flow field, after which the beam was then passed through beam reduction relay optics consisting of a 750mm focal length plano-convex lens and a 250mm focal length plano convex lens, resulting in a 3X beam reduction. For the transverse profile, shadowgraph images were recorded on a Phantom v2512 highspeed camera at a frame rate of 160,000 fps with a resolution of 208 x 512, an exposure time of 0.4μs, and a pixel size of 28μm.

C. Coaxial Image Path

While the TIP portion of the experimental setup was nearly identical to that of previous work[15], the purpose of the CIP (light green) was to image the LIB flowfield's coaxial profile. To our knowledge, no other experimental work has imaged the coaxial LIB flowfield, and most numerical investigations assume an axisymmetric profile for a laser
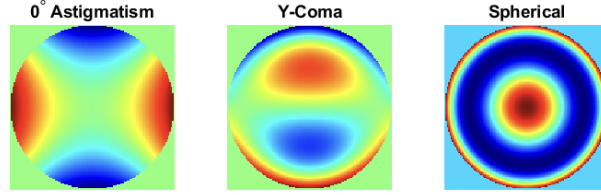
4

Fig. 4   Zernike phase aberrations tested for this research.

pulse with a Gaussian intensity distribution and a planar wavefront. This is obviously not the case for a laser pulse with significant phase aberration that causes non-uniform raidal intensity distributions. Specifically, Zernike polynomials are orthogonal on the unit disk, so it would be incorrect to assume that the Zernike phase aberrations have no significant influence on the radial or angular velocity of the laser spark flowfield.

Similar to the TIP, the CIP used a 250mm focal length plano-convex lens to expand the beam and a 500mm plano-convex lens to collimate the beam after splitting off from the polarizing beamsplitter. The CIP beam was then steered onto the dichroic mirror, reflecting in-line with the SP laser pulse, before being reflected off another dichroic mirror. The beam was then reduced in the same way as the TIP beam before being sent to a Phantom v1611 highspeed camera. The CIP camera recorded shadowgraph images with at a frame rate of 160,000fps, a pixel resolution of 208 x 256, and an exposure time of 0.4μs. The pixel size for the v1611 is the same as that of the v2512.

Table 1   Data matrix for experiment with phase aberrations tested.

Phase Aberration	Magnitude Range(μm)
0° Astigmatism	[-3.74, 3.74]
45° Astigmatism	[-3.80, 3.80]
X-Coma	[-3.50, 3.50]
Y-Coma	[-3.42, 3.42]
X-Trefoil	[-3.44, 3.44]
Y-Trefoil	[-3.44, 3.44]
Spherical	[-1.95, 1.95]

D. Data Acquisition

Synchronization of the data was achieved using the Q-Switch output pulse of the SP laser control unit to trigger both the TIP and CIP cameras via BNC cables connected to the cameras' trigger inputs. A -500ns delay between the output of the Q-Switch signal to the cameras and the laser head was set to ensure that the first frames of both cameras capture the very beginning of the flowfield. An additional BNC connector was used to synchronize the first frames of both cameras to prevent flowfield mismatch between the TIP and CIP.

The experimental data matrix for the aberrations tested are shown in Table.1. To relate the flowfield quantities (velocity and vorticity) to the spark-absorbed energy, the energy pulse meter was used to collect and average reading of the remaining energy after the laser spark was created. The percent difference between the pre-spark laser energy of 181mJ and the post-spark laser energy, averaged over 500 spark instances, was taken for each aberration tested using the DM. During the experiments, instantaneous pulse energies were recorded post-spark, and assigned to their respective flowfields. A total of 100 sparks were captured for each aberration tested, with approximately 2000-3000 individual frames (12.5ms-18.75ms).

IV. Optical Flow

Recent experimental work[Noel and Rennie] has shown that accurate and well-resolved spatiotemporal measurements of complex flowfields created as a result of laser-induced breakdown can be obtained from optical flow methods applied to standard flow visualization techniques. Whereas previous experimental work has found difficulty in producing good

temporal resolution[22,23], and numerical work is restricted to simple, axisymmetric cases, the optical flow method makes possible an in-depth analysis of the flowfield produced by laser-induced breakdown.

A. Optical Flow Constraint Equation

Most optical flow algorithms are formulated to solve the optical flow constraint equation (OFCE), which relates the apparent shift in image intensity between two images to the velocities that create that shift. Consider a time-series of image data that captures the motion of a non-stationary object. With sufficient temporal resolution, the depicted motion may appear to the naked eye as stationary. This mean that, for a pixel located at (x_0, y_0), the image intensity in an infinitesimally small area around that pixel location remains constant between some time, t_0, and some time $t_0 + \delta t$. This "brightness constancy" constraint may be mathematically expressed as,

$$I(x_0 + \delta x, y_0 + \delta y, t_0 + \delta t) \approx I(x_0, y_0, t_0) \tag{1}$$

where $I(x_0, y_0, t_0)$ is the image intensity at location (x_0, y_0) at time t_0. Taking the first-degree Taylor expansion of the left-hand side yields,

$$I(x_0, y_0, t_0) + \frac{\partial I}{\partial x}\delta x + \frac{\partial I}{\partial y}\delta y + +\frac{\partial I}{\partial t}\delta t \approx I(x_0, y_0, t_0) \tag{2}$$

Reducing further and dividing through by δt,

$$I_x u + I_y v + I_t = 0 \tag{3}$$

where the subscripts denote derivative values. Eq. (3), formally known as the Optical Flow Constraint Equation (OFCE), assumes that the image intensity or within a small region around a pixel is constant between consecutive images. With one equation and two unknowns, the OFCE is ill-posed. Common solutions to the OFCE either directly solve for the local optical flow within some small window, or incorporate an assumption about the global organization of the solution to provide closure to the OFCE, as in typical variational formulations to be discussed.

B. Horn-Schunck Method

The well-known Horn-Schunck method[16] was employed to handle the calculation of the projected motion flowfield. Although there exist optical flow methods specifically designed for fluid flow[17] which will be explored in future work, the Horn-Schunck method is chosen for its simplicity and ease of implementation. Horn and Schunck closed the system of equations by assuming that the solution to the OFCE is globally smooth, which is enforced by adding a constraint on the acceptable values of the velocity gradients. By solving this closed system of equations, a dense optical flow field can be recovered from the apparent projected motion between consecutive frames. This method is implemented by way of a first-order Tikhonov regularization of the form,

$$J_{reg}(\vec{u}) = \alpha^2 \int_{\Omega} (||\nabla u||^2 + ||\nabla v||^2)d\Omega \tag{4}$$

The global energy functional to be minimized can then be expressed as,

$$J(\vec{u}) = \int_{\Omega} (I_x u + I_y v + I_t)^2 d\Omega + \alpha^2 \int_{\Omega} (||\nabla u||^2 + ||\nabla v||^2)d\Omega \tag{5}$$

where the first term is coined the "data term", which relies on the measured image gradients and the second term is the "regularization term" which embodies assumptions about the spatial organization of the solution. The Lagrange multiplier, α, is the regularization parameter that controls the relative importance between the data term and the regularization term. In this case, α acts as a diffusive parameter, where larger values of alpha yield smoother flow with smaller velocity gradients. The associated Euler-Lagrange Equations reads,

$$I_x(I_x u + I_y v + I_t) - 2\alpha^2 \nabla^2 u = 0 \tag{6}$$

$$I_y(I_x u + I_y v + I_t) - 2\alpha^2 \nabla^2 v = 0 \tag{7}$$

Placing a constraint on the acceptable values of the velocity gradients in the weak formulation shown in Eq. (5) incorporates information from the Laplacian values of the velocity in the strong formulations presented in Eqs. (6) and (7). The Laplacian is then estimated using finite difference formulations as in [16],

$$\nabla^2 u = 4(\bar{u} - u) \tag{8}$$

6

$$\nabla^2 v = 4(\bar{v} - v) \tag{9}$$

where the overbar denotes an averaging of the first-order neighborhood of points. The convolutional kernel used in flow averaging depends on the selection of finite difference kernel, where the original Horn-Schunck formulation used a second-order central difference kernel convolved with a Gaussian kernel. What this means is that the velocity value at every point in the image is influenced by a weighted average of the surrounding pixels, scaled by the regularization parameter alpha. Equations (6) and (7) compose a system of equations whose solution is pursued through a fixed-point iterative scheme,

$$u^{k+1} = \bar{u}^k - \frac{(I_x \bar{u}^k + I_y \bar{v}^k + I_t)}{4\alpha^2 + I_x^2 + I_y^2} \tag{10}$$

$$v^{k+1} = \bar{v}^k - \frac{(I_y \bar{u}^k + I_y \bar{v}^k + I_t)}{4\alpha^2 + I_x^2 + I_y^2} \tag{11}$$

where superscript k denotes the current iteration. The velocities may be initialized to 0 for the first iteration or may be initialized to an estimate of the velocities from a previous time step.
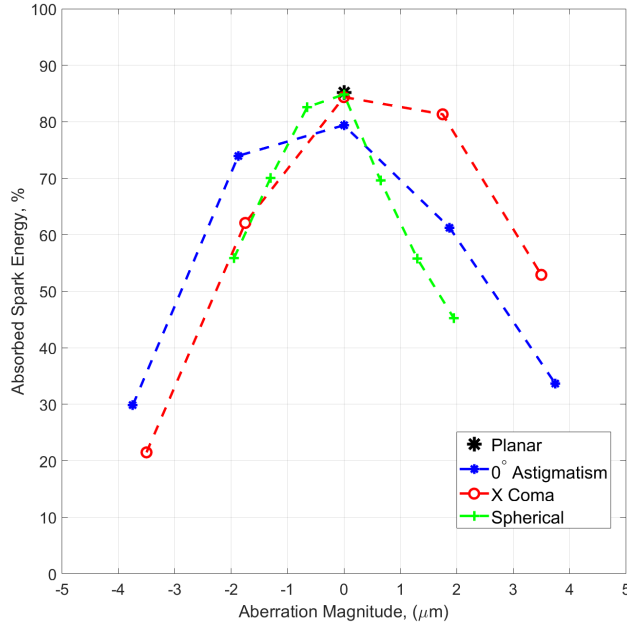

Fig. 5 Percentages of laser energy absorbed by spark for each Zernike phase aberration presented.

V. Results and Discussion

Figure5 shows the percentage of energy absorbed by the spark for each aberration at each level. For the average input laser energy of 181mJ, the amount of energy absorbed by the spark significantly decreases with the magnitude of the Zernike phase aberration. This behavior is currently thought to have two main contributors. First, phase deviations from a planar wavefront inhibit the focus-ability of the pulse, reducing the laser intensity in the focal region. Both the condition of gas breakdown as well as the growth of the plasma spark are dependent on the laser intensity,

$$I_{laser} = \frac{E_{pulse}}{t_{pulse} * A_w} \tag{12}$$

where E_{pulse} is the laser pulse energy, t_{pulse} is the laser pulse duration and A_w is the cross-sectional area of the pulse at its tightest focus. The smallest area attainable for any laser beam limited only by diffraction is one with a Gaussian
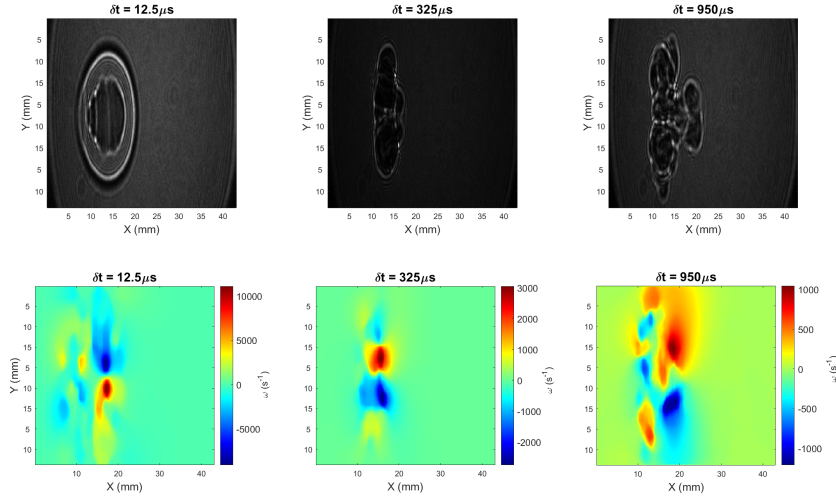
7

Fig. 6   Shadowgraph (top row) images of the flowfield caused by LIB with no phase aberration at three distinct time delays after the laser pulse in the TIP field of view with an energy of 135.39mJ. Corresponding vorticity profiles (bottom row) are also given. Laser is incident from the right.

intensity profile and planar wavefront. The second contribution is how the presence of significant phase aberrations create common regions of focus along the optical path (z-axis). Regions of the laser pulse that experience positive phase shifts from the planar wavefront will be focused further away from the nominal breakdown location, which is approximately equal to the focal length of the focusing lens. Conversely, regions that experience negative phase shifts will be focused closer to the laser source. As will be discussed in more detail below, the different Zernike phase aberrations all have unique flowfields that vary with the magnitude of aberration for each mode.

A. Planar

Figure6 shows a single realization of the transverse shadowgraph profiles (top) of a spark with a planar wavefront at three different times after the laser pulse, accompanied by the corresponding vorticity profiles (bottom) for three distinct time delays after the laser pulse. This case corresponds to that of a flat DM, where the voltage applied is even across all actuators. From Fig.4, we have that roughly 85% of the laser pulse energy is absorbed by the spark; for the flowfields presented in Fig.6 and Fig.7, the absorbed energy is approximately 135.39mJ. The transverse profile of the planar spark shows the expected flow behavior; two counter-rotating toroidial vortices that eject a third vortex at a later time. This flowfield behavior is one that is ubiquitously observed in past experimental and numerical works. The peak vorticity is on the order of $10^4 s^{-1}$ at 12.5μs after the laser pulse, which lies within good agreement with other experimental results, such as that of Koll et al.[9] who used a pulse laser operating at 532nm. Still, it is difficult to compare as few works look into the flowfield development of LIB from an experimental perspective. Furthermore, as there is currently no study to our knowledge of the behavior of the flowfield with respect to laser parameters such as wavelength, focusing optics, and energy input, a direct comparison using scaling arguments is not yet possible.

The coaxial profile for the planar spark is presented in Fig.7, where the key quantity of interest is the radial velocity. While most numerical simulations assume an axisymmetric distribution for the velocities in which there is no angular velocities and only pure radial motion in the plane perpendicular to the laser pulse propagation, the experimental results show that this is only really true in very short time delays after spark generation. The cause of deviation from the axisymmetric assumption may be due to small deviations in the assumed planar wavefront, these small deviations are almost impossible to remove entirely from an experimental standpoint. Furthermore, small perturbations in the laser energy distribution across the beam profile may lead to imbalances in the growth of the plasma, presenting a destabilizing effect on the resulting flow. Therefore, the assumption of axisymmetric flow can be regarded as the ideal case for a planar wavefront. In reality, a three-dimensional, complicated flowfield is typically observed.
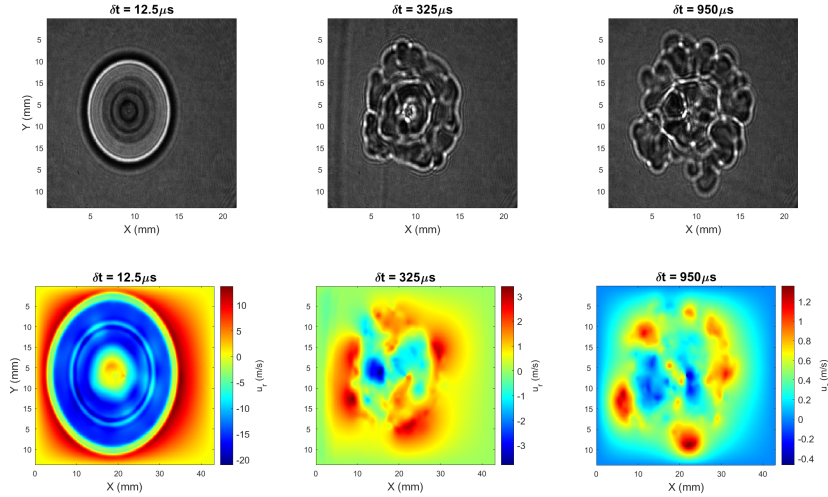
8

Fig. 7   Shadowgraph (top row) images of the flowfield caused by LIB with no phase aberration at three distinct time delays after the laser pulse in the CIP field of view with an energy of 135.39mJ. Corresponding radial velocity profiles (bottom row) are also given. Laser is incident out of the plane.

B. 0 Deg. Astigmatism

The transverse flowfield for a spark with 0°astigmatism is shown in Fig.8. The amplitude of the aberration shown here is approximately -3.74μm of astigmatic aberration and the spark is estimated to have absorbed 59.06mJ of the laser pulse energy. In comparison to the planar spark, the astigmatism spark peak vorticity amplitude is an order of magnitude less than that of the planar spark in the TIP field of view. This, again, is due to how phase aberrations decrease the focal-region intensity by increasing the focal region area. In the first frame with time delay of 12.50μs, both the primary and secondary toroidal vortices are approximately equal in magnitude, hinting at some redistribution of energy along the plasma length due to the astigmatic aberration, although the mechanism is yet to be fully understood. Additionally, the presence of astigmatism does not seem to inhibit or enhance the properties of the ejection vortex.

In the CIP field of view, the effect of the non-planar wavefront is easily seen. In comparison to the radial velocity profile shown in Fig.7, the radial velocity profile presented in Fig.9 shows a non-symmetric distribution at early times. At later times, this asymmetry becomes more apparent and presents as a bulk expansion that is biased to the left of the CIP field of view. At later times still, this bulk motion takes on a more oblique behavior. The exact relationship between the amount of aberration and the specific flowfield behavior is still yet to be uncovered.

C. Y Coma

The effect of Zernike Y-Coma aberration on the transverse profile of the flowfield is shown in Fig.10, where the amplitude of the aberration is approximately -3.42μm of aberration and approximately 75.09mJ of the laser energy is absorbed by the plasma spark. In the early times, the flow is very similar to the planar wavefront case, where there are two main toroidal vortices with a maximum vorticity on the order of $10^4 s^{-1}$. However, further development of the flow shows that the development of the ejection vortex is attenuated, favoring almost purely radial expansion.

The CIP field of view shown in Fig.11, the center of the radial velocity profile shows a bias towards the +y direction, which is also observed in later times as well. The current hypothesis is that comatic aberrations create a local defocusing of the laser energy, creating an imbalance about a common axis (in this case, the x-axis) in the focal region during breakdown. Imbalance in the laser energy causes an imbalance in the plasma profile, which then creates an imbalance in the flow velocity. This suggests that altering the phase of a high-energy pulse may give hyper-specific control to the local flow features generated by LIB.
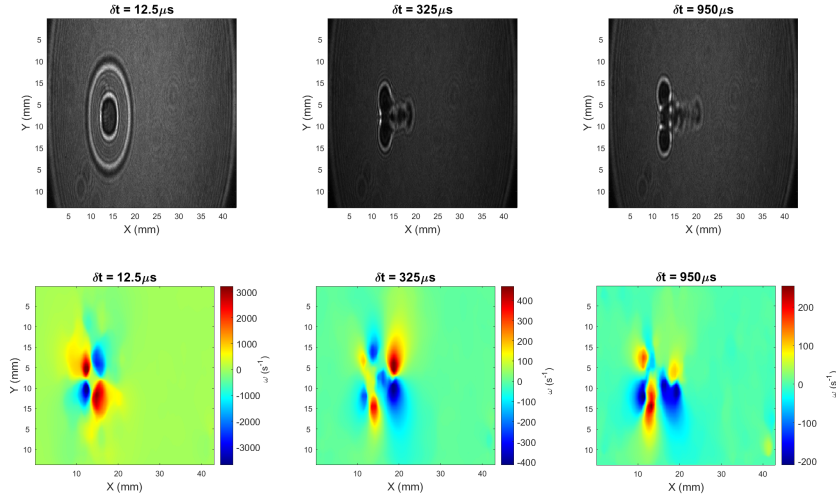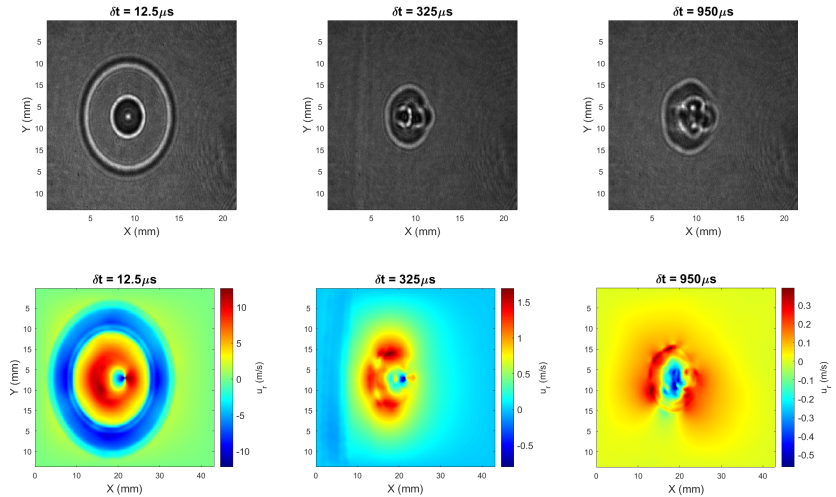
9

Fig. 8   Shadowgraph (top row) images of the flowfield caused by LIB with $0°$ Astigmatic phase aberration at three distinct time delays after the laser pulse in the TIP field of view. Corresponding vorticity profiles (bottom row) are also shown. The estimated aberration magnitude is -3.74μm with a spark energy of approximately 59.06mJ. Laser is incident from the right.

Fig. 9   Shadowgraph (top row) images of the flowfield caused by LIB with $0°$ Astigmatic phase aberration at three distinct time delays after the laser pulse in the CIP field of view. Corresponding radial velocity profiles (bottom row) are also given. The estimated aberration magnitude is -3.74μm with a spark energy of approximately 59.06mJ. Laser is incident out of the plane.

D. Spherical

Spherical aberration has perhaps the most "expressive" flowfields of the flows shown here, featuring two individual sparks, as shown in the TIP field of view in Fig.12. The cause of this is readily identifiable; spherical aberration takes radial sections of the laser pulse and creates different focal points spread out along the SP's focal region, which creates multiple sparks with accompanying shocks. Although, only -1.3μm of spherical aberration is used with 75.71mJ of energy, a unique flowfield containing multiple sets of toroidal vorticies interacting with each other is formed, quickly decaying into turbulent motion, as seen in later times. In LIB with no phase aberration, the shock-generated vorticity is
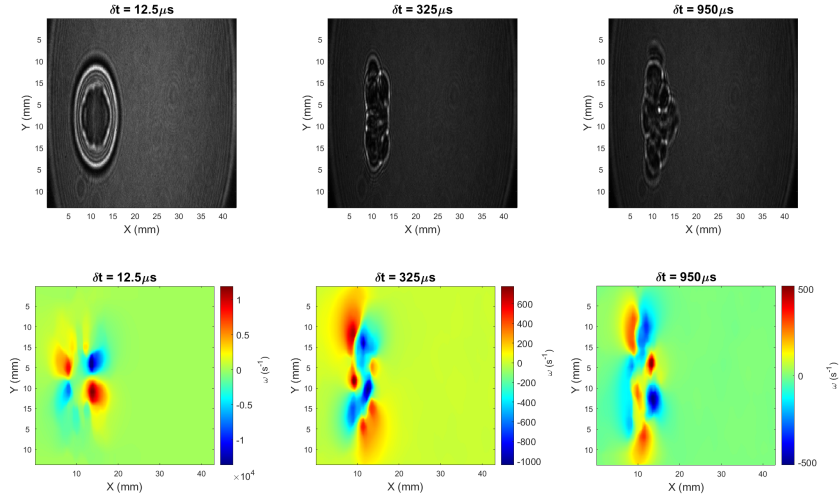
10

Fig. 10   Shadowgraph (top row) images of the flowfield caused by LIB with Y-Coma phase aberration at three distinct time delays after the laser pulse in the TIP field of view. Corresponding vorticity profiles (bottom row) are also shown. The estimated aberration magnitude is -3.42μm with a spark energy of approximately 75.09mJ. Laser is incident from the right.
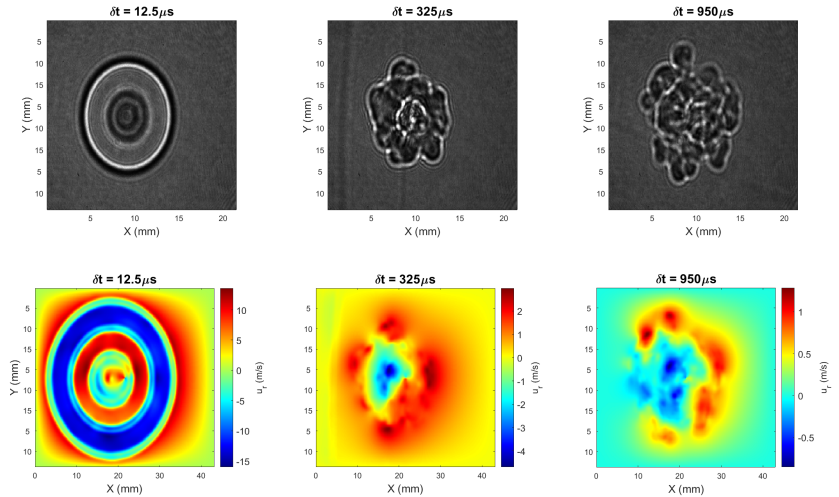

Fig. 11   Shadowgraph (top row) images of the flowfield caused by LIB with a planar wavefront at three distinct time delays after the laser pulse in the CIP field of view. The estimated aberration magnitude is -3.42μm with a spark energy of approximately 75.09mJ. Corresponding radial velocity profiles (bottom row) are also given.

heavily attenuated by the baroclinic torque due to the pressure gradient of the rarefaction wave and the density gradient of the high-temperature gas kernel, as explained in Wang et al.[18]. In the case of LIB with spherical aberration, the presence of two interacting shocks seems to create vorticity due to an additional, "mutual" baroclinic effect owing to the misalignment of the density and pressure gradients between each shock. Additionally, the presence of both shocks seems to overtake the attenuation due to baroclinic torque in the transverse plane, although this has to be further investigated. The coaxial profile, shown in 13, does not seem to produce any unique features that strongly differ from that shown in the planar wavefront.
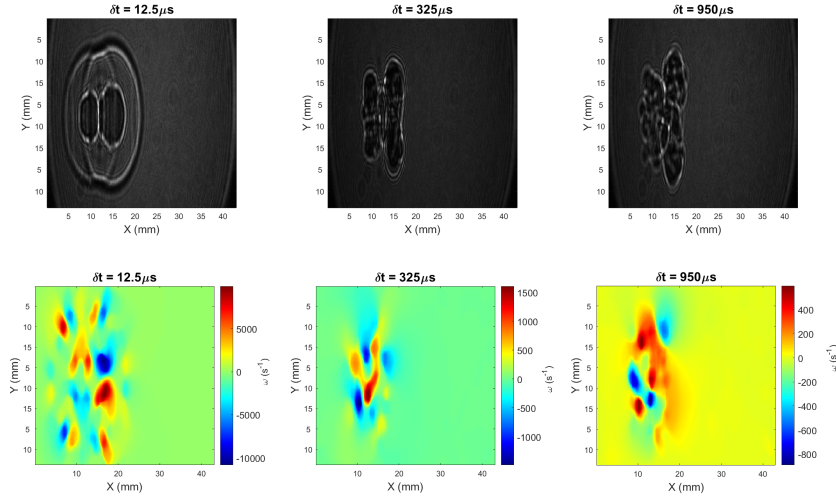
11

Fig. 12   Shadowgraph (top row) images of the flowfield caused by LIB with Spherical phase aberration at three distinct time delays after the laser pulse in the TIP field of view. The estimated aberration magnitude is -1.3μm with a spark energy of approximately 75.71mJ. Corresponding vorticity profiles (bottom row) are also shown.Laser is incident from the right.
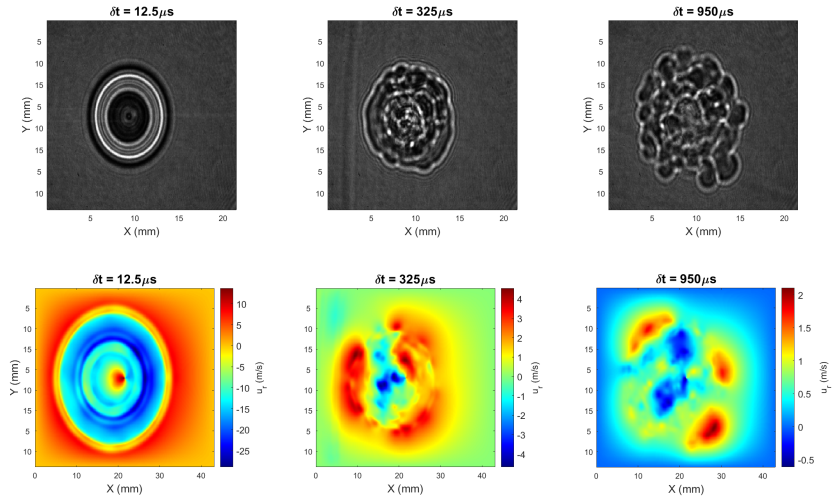

Fig. 13   Shadowgraph (top row) images of the flowfield caused by LIB with Spherical phase aberration at three distinct time delays after the laser pulse in the CIP field of view. The estimated aberration magnitude is -1.3μm with a spark energy of approximately 75.71mJ. Corresponding radial velocity profiles (bottom row) are also given.

VI. Conclusions and Future Work

The effect of phase aberration on the spatiotemporal development of the flowfield caused by laser-induced breakdown is investigated. Three primary aberrations are compared against the baseline case of a planar phase; Zernike 0° Astigmatism, Zernike Y-Coma, and Zernike Spherical aberrations. The phase aberrations are produced by using a deformable mirror (DM) and a unique experimental setup is utilized to capture orthogonal shadowgraph projections of the resulting flowfield. The Horn-Schunck optical flow algorithm is then used to process the flowfields, producing quantitative results for the flow velocities. It is shown that the presence of phase aberration is capable of producing

12

unique flowfields that are controllable by the deformable mirror. The ability to specify flow features within a region of space bodes well for flow control applications, especially turbulent mixing applications where the control of vorticity is of key importance.

Out of the many instances were recorded, flowfields at a select few time delays after the high-energy laser pulse are investigated. Future work will focus on accurately capturing the full flow velocities over the entire time history and performing a more robust analysis of the flowfields. Additionally, as the Horn-Schunck method is not specifically designed for fluid flow, further investigation into optical flow for fluid applications will be performed, which should yield better results. Furthermore, as only a single phase aberration magnitude was presented for each Zernike polynomial investigated here, future work will also seek to establish a relationship between the phase of the high-energy laser pulse, and the flowfield that is created, which should aide in the development of new numerical methods that can be used to further advance and promote LIB research as a method of flow control.

VII. Acknowledgements

References

[1] Bradley, D., Sheppard, C., Suardjaja, I., and Woolley, R., "Fundamentals of high-energy spark ignition with lasers," *Combustion and Flame*, Vol. 138, No. 1, 2004, pp. 55–77. https://doi.org/https://doi.org/10.1016/j.combustflame.2004.04.002, URL https://www.sciencedirect.com/science/article/pii/S0010218004000914.

[2] Phuoc, T. X., "Laser spark ignition: experimental determination of laser-induced breakdown thresholds of combustion gases," *Optics Communications*, Vol. 175, No. 4, 2000, pp. 419–423. https://doi.org/https://doi.org/10.1016/S0030-4018(00)00488-0, URL https://www.sciencedirect.com/science/article/pii/S0030401800004880.

[3] Lee, G. S., Liu, Q., Baccarella, D., Elliott, G. S., and Lee, T., *A Novel Supersonic Injection Scheme for Laser Induced Breakdown Ignition*, ???? https://doi.org/10.2514/6.2018-4286, URL https://arc.aiaa.org/doi/abs/10.2514/6.2018-4286.

[4] Adelgren, R. G., Yan, H., Elliott, G. S., Knight, D. D., Beutner, T. J., and Zheltovodov, A. A., "Control of Edney IV Interaction by Pulsed Laser Energy Deposition," *AIAA Journal*, Vol. 43, No. 2, 2005, pp. 256–269. https://doi.org/10.2514/1.7036, URL https://doi.org/10.2514/1.7036.

[5] Zheltovodov, A., Pimonov, E., and Knight, D., *Energy Deposition Influence on Supersonic Flow Over Axisymmetric Bodies*, ???? https://doi.org/10.2514/6.2007-1230, URL https://arc.aiaa.org/doi/abs/10.2514/6.2007-1230.

[6] Kim, J.-H., Matsuda, A., Sakai, T., and Sasoh, A., "Wave Drag Reduction with Acting Spike Induced by Laser-Pulse Energy Depositions," *AIAA Journal*, Vol. 49, No. 9, 2011, pp. 2076–2078. https://doi.org/10.2514/1.J051145, URL https://doi.org/10.2514/1.J051145.

[7] Khamseh, A. P., Kiriakos, R. M., and DeMauro, E. P., *Towards Trajectory Control of a Supersonic Projectile Using Laser Energy Deposition*, ???? https://doi.org/10.2514/6.2019-1347, URL https://arc.aiaa.org/doi/abs/10.2514/6.2019-1347.

[8] Bright, A., Tichenor, N., Kremeyer, K., and Wlezien, R., "Boundary-Layer Separation Control Using Laser-Induced Air Breakdown," *AIAA Journal*, Vol. 56, No. 4, 2018, pp. 1472–1482. https://doi.org/10.2514/1.J055272, URL https://doi.org/10.2514/1.J055272.

[9] Koll, M., Elliott, G. S., and Freund, J., *Particle Image Velocimetry of a Nano-Second Laser Induced Breakdown in Air*, ???? https://doi.org/10.2514/6.2020-2047, URL https://arc.aiaa.org/doi/abs/10.2514/6.2020-2047.

[10] Boguszko, M., and Elliott, G. S., "On the use of filtered Rayleigh scattering for measurements in compressible flows and thermal fields," *Experiments in Fluids*, Vol. 38, No. 1, 2005, pp. 33–49. https://doi.org/10.1007/s00348-004-0881-4, URL https://doi.org/10.1007/s00348-004-0881-4.

[11] Kojima, H., Takahashi, E., and Furutani, H., "Breakdown plasma and vortex flow control for laser ignition using a combination of nano- and femto-second lasers," *Opt. Express*, Vol. 22, No. S1, 2014, pp. A90–A98. https://doi.org/10.1364/OE.22.000A90, URL https://opg.optica.org/oe/abstract.cfm?URI=oe-22-101-A90.

[12] Apeksimov, D. V., Geints, Y. E., Zemlyanov, A. A., Kabanov, A. M., Oshlakov, V. K., Petrov, A. V., and Matvienko, G. G., "Controlling TW-laser pulse long-range filamentation in air by a deformable mirror," *Appl. Opt.*, Vol. 57, No. 33, 2018, pp. 9760–9769. https://doi.org/10.1364/AO.57.009760, URL https://opg.optica.org/ao/abstract.cfm?URI=ao-57-33-9760.

[13] Glumac, N., and Elliott, G., "The effect of ambient pressure on laser-induced plasmas in air," *Optics and Lasers in Engineering*, Vol. 45, No. 1, 2007, pp. 27–35. https://doi.org/https://doi.org/10.1016/j.optlaseng.2006.04.002, URL https://www.sciencedirect.com/science/article/pii/S0143816606001059.

[14] Bindhu, C., Harilal, S., Tillack, M., Najmabadi, F., and Gaeris, A., "Energy Absorption and Propagation in Laser-Created Sparks," *Appl. Spectrosc.*, Vol. 58, No. 6, 2004, pp. 719–726. URL https://opg.optica.org/as/abstract.cfm?URI=as-58-6-719.

[15] Noel, Z. A., and Rennie, M. R., *Experimental Investigation of Toroidal Vortices in Laser-Induced Breakdown Plasma*, ???? https://doi.org/10.2514/6.2022-2259, URL https://arc.aiaa.org/doi/abs/10.2514/6.2022-2259.

[16] Horn, B. K., and Schunck, B. G., "Determining optical flow," *Artificial Intelligence*, Vol. 17, No. 1, 1981, pp. 185–203. https://doi.org/https://doi.org/10.1016/0004-3702(81)90024-2, URL https://www.sciencedirect.com/science/article/pii/0004370281900242.

[17] Liu, T., and Shen, L., "Fluid flow and optical flow," *Journal of Fluid Mechanics*, Vol. 614, 2008, pp. 253 – 291. https://doi.org/10.1017/S0022112008003273.

[18] Wang, J. M., Buchta, D. A., and Freund, J. B., "Hydrodynamic ejection caused by laser-induced optical breakdown," *Journal of Fluid Mechanics*, Vol. 888, 2020, p. A16.